Carbon 161 (2020) 880–891

Contents lists available at ScienceDirect

Carbon

journal homepage: www.elsevier.com/locate/carbon

Scalable and controlled creation of nanoholes in graphene by microwave-assisted chemical etching for improved electrochemical properties

Dini Wang [a], Rui Dai [a], Xing Zhang [b], Lei Liu [a], Houlong Zhuang [a], Yongfeng Lu [c], Yan Wang [b], Yiliang Liao [b], Qiong Nian [a, *]

[a] School of Engineering for Matter, Transport and Energy, Arizona State University, Tempe, AZ, 85287, USA
[b] Department of Mechanical Engineering, University of Nevada, Reno, NV, 89557, USA
[c] Department of Electrical & Computer Engineering, University of Nebraska-Lincoln, Lincoln, NE, 68588, USA

ARTICLE INFO

Article history:
Received 2 January 2020
Received in revised form
20 January 2020
Accepted 22 January 2020
Available online 23 January 2020

ABSTRACT

Nanoholes on the basal plane of graphene can provide abundant mass transport channels and chemically active sites for enhancing the electrochemical performance. However, current thermal chemical etching processes to manufacture these nanoholes commonly suffer from insufficient process efficiency, scalability and controllability, due to the conventional bulk heating strategy lacks capability to promote the etching reactions. To address this issue, a novel process is developed using microwave irradiation to promote and control the chemical etching of graphene. In this process, the microwave can induce a selective heating of graphene in the liquid solution and then facilitate the etching reactions occurring on the graphene-etchant interface. Applying this strategy, a remarkable reduction of processing time from hour-scale to minute-scale compared to the conventional approaches have been achieved with the control of the population and area percentage of nanoholes on the graphene basal plane. Density functional theory and molecular dynamics simulations revealed that the formation of nanoholes originated from the cyclic etchant oxidation process occurring at the edge-sites atoms around pretreated vacancies on graphene basal plane. The obtained holey graphene oxide sheets exhibit excellent capacitive performance and electrochemical catalytic activity due to the improvements in the accessible surface area, ion diffusion, and heterogeneous charge transfer.

1. Introduction

As one of the most important two dimensional (2D) materials, graphene has attracted enormous attention for being utilized as the active component or conductive additive in electrochemical electrodes of batteries, supercapacitors, catalysts, and sensors, due to its superior electrochemical activity, high electrical conductivity, and large specific surface area [1–3]. Nevertheless, an inevitable limitation of graphene-based electrodes on mass transport is that ions or molecules cannot directly travel across the basal plane of a graphene sheet. Hence, the mass traveling paths in graphene sheets are tortuous and lengthened [4,5]. This reduces the accessible surface area for absorbing substances, such as electrolytes or reactants, leading to the sluggish diffusion kinetics and hindering the performance improvement brought by graphene [5,6]. This issue can be even worse if the graphene sheets are densely assembled with high mass loadings (e.g., >10 mg cm^{-2}), or start self-wrapping and re-stacking [6,7]. A potential solution to this issue has been proposed of creating nanoholes on the basal planes of graphene sheets. These nanoholes serve as the mass transport channels that allow ions or molecules to directly transport so that the electrolyte accessible surface area of graphene sheets are restored [4,5]. Moreover, the hole-making process would introduce extended edge sites to the graphene basal plane around where the nanoholes are created. These edge-site carbon atoms are more chemically active than the in-plane ones [8,9] and therefore can improve the electrochemical activity of graphene electrodes, making holey graphene very attractive in various electrochemical applications [10–17]. For instance, Xu et al. reported a holey graphene electrode with an ultrahigh gravimetric capacitance of

* Corresponding author.
E-mail addresses: qiong.nian@asu.edu, qnian@asu.edu (Q. Nian).

https://doi.org/10.1016/j.carbon.2020.01.076
0008-6223/

310 F g^{-1}, about 1.5 times higher than that of the pristine graphene [5]. Sun et al. found that by incorporating holey graphene with transition metal oxides, the nanocomposite can realize the outstanding rate capability and specific capacity with a mass loading high enough for practical applications [10].

Despite the highly promising electrochemical characteristics of holey graphene, the manufacture of this material is challenging due to the structural inertness of graphene lattice and the high covalent bond strength among the sp^2-hybridized carbon atoms. For these reasons, holey graphene is generally fabricated from graphene oxide (GO) that has weaker sp3 bonds in the lattice [18], which can be chemically etched to form through-the-thickness nanoholes. Various fabrication methods have been reported, including steam etching [19], refluxing or sonicating with nitric acid [12,20], chemical activation [21], catalytic oxidation [22,23], photocatalytic oxidation [24], etc. However, these methods designed for specific applications often suffer from issues such as chemical contamination or deterioration to the graphene structure. To tackle this challenge, Duan et al. recently developed an approach to fabricating holey graphene by heating GO solution with hydrogen peroxide etchant followed by reduction process, through which they obtained products with both high specific surface area (1560 m^2 g^{-1}) [5] and electrical conductivity (2030 S m^{-1}) [25]. This simple and green method has been prevalent for holey graphene fabrication since then [15–17,26–28]. However, it is still time- and energy-consuming, since a constant bulk heating for several hours at around 100 °C is required to obtain products, and a considerable amount of energy can be dissipated to the ambient environment. The low process efficiency is attributed to the fact that bulk heating process lacks the capability to promote graphene-etchant reactions in their interface. Besides, the long-period treatment under the boiling temperature can lead to the decomposition of hydrogen peroxide molecules before they react with GO sheets.

Alternative methods for holey graphene fabrication have been proposed, such as heating and oxidizing in air [13,14,29–31] or direct exfoliation from graphite [32,33]. Despite their potential in fabrication scalability, these solid-phase methods have an inherent issue on dispersing graphene materials and etchants to ensure the homogeneity of chemical reactions. The inhomogeneous reactions consequently lead to the non-uniform formation of nanoholes and bring difficulty in quality control. On the contrary, the liquid-phase methods mentioned above are not only favorable to obtain holey graphene with more uniform properties but also superior in process continuity. This is because that the fabrication of GO, which is the starting material for holey graphene fabrication (except for the direct exfoliation method [32,33]), is dominated by the liquid-phase route that has been offering low-cost graphene products for a broad range of applications during over a decade's growth of the graphene industry [34]. In this respect, a fast, scalable, controllable, cost-effective, and solution-based fabrication method of holey graphene is still highly desirable. In addition, the mechanism of nanoholes nucleation and growth also deserves a systematical study for controlling the population and size of the holes on the graphene basal plane.

Herein, this paper reports a novel method for holey graphene fabrication via microwave-assisted chemical etching (MACE) of the GO solution. This process couples vigorous chemical attack with rapid electromagnetic wave irradiation to reduce the processing time from hour-scale to minute-scale. The mechanism of MACE process is revealed through a comparison study emphasizing on the in situ heat generation and selective heating of GO sheets in the solution under microwave irradiation. Moreover, a simple two-step strategy is developed to effectively control the population and area percentage of the nanoholes on the holey graphene sheets. The microstructural evolutions during each step of fabrication, including the changes in the atomic ratio, defect density, and the number of functional groups, are analyzed by various characterization techniques to help understanding the formation and growth mechanisms of nanoholes on GO sheets. Multiscale simulations are employed to unveil the thermal chemical mechanism during the fabrication of holey graphene. The capacitive performance and electrochemical catalytic activity of the holey graphene sheets are evaluated. By adjusting the microstructure of nanoholes via the two-step strategy, we further demonstrate the versatile potentials of this material with tunable electrochemical properties.

2. Experimental section

2.1. Fabrication of holey graphene

The 3 mg mL^{-1} GO aqueous solution (3 mL) was added into a glass tube sealed by a PTFE cap and pretreated by irradiating in a microwave reactor (Anton Paar Monowave 400, 2.45 GHz) at a constant power of 50 W for 90–360 s with magnetic stirring at a speed of 600 rpm. The GO aqueous solution was first prepared using graphite flakes (50+ mesh, Sigma-Aldrich) by the improved Hummer's method [35]. The setup of the microwave reactor is illustrated in Fig. S1. Briefly, an infrared thermometer recorded the temperature profile per second, and a pressure sensor collected the variation of pressure inside the reaction tube. Compressed air flow was used to cool down the solution to room temperature after microwave irradiation. Then, the pretreated GO solution and hydrogen peroxide were mixed in a reaction tube with a volume ratio of 5:2. The mixture was irradiated in the microwave reactor at a constant power of 50 W for 45–180 s. After cooling, the solution was centrifuged at 12 k rpm for 15 min to remove residual hydrogen peroxide. The precipitate was then re-dispersed in deionized water to form the holey GO (hGO) aqueous solution. The hGO aqueous solution was irradiated in the microwave reactor to 220 °C and held for 90 s to obtain the reduced holey GO (rhGO) aqueous solution.

2.2. Calculation methods

We used the Vienna Ab-initio Simulation Package for all the density functional theory (DFT) calculations [36]. The plane waves used in the calculations had an energy cutoff of 500 eV. We also used the Perdew-Burke-Ernzerhof functional [37] and the corresponding version of standard potential data sets generated by the projector augmented-wave method [38,39]. All the supercells have a vacuum spacing of 18.0 Å and a single k point (Γ) was used for the k-point sampling. The atomic coordinates were fully optimized until the forces were converged to 0.01 eV/Å. In the molecular dynamics (MD) calculations, the reactive force-field (ReaxFF) is utilized to describe the bond association/disassociation process during the thermal annealing of GO. Structure optimization with ReaxFF was performed at room temperature. A Berendsen thermostat with a damping parameter of 100 time-steps was used to control the system temperature. The time step is 0.05 fs. Molecular by-products released from the GO sheet were removed periodically every 10 fs to mimic the experimental reduction environment against vacuum.

2.3. Microstructure characterization

The morphologies of graphene sheets were characterized on an aberration-corrected transmission electron microscopy (TEM, FEI Titan 300/80) using the electron beam with an acceleration voltage of 300 kV. The atomic force microscopy (AFM) was performed on a Bruker Multimode 8 system using the contact mode. Chemical

compositions of graphene samples were analyzed using the X-ray photoelectron spectroscopy (XPS, VG Escalab 220i-XL) with a monochromatic Al K-alpha source. Raman spectra were collected using a 532-nm laser. Each spectrum was scanned 10 times with durations of 1 s per scan. The spectrum center and filter grating were 2050 cm^{-1} and 600 g mm^{-1}, respectively.

2.4. Electrochemical measurements

The electrochemical measurements were carried out on a CH Instruments 660 E workstation at ambient condition using a three-electrode setup that included a 0.5 mm Pt wire as the counter electrode, a Ag/AgCl reference electrode in 1 M KCl (+0.235 V vs. standard hydrogen electrode), and a glassy carbon working electrode (GCE). The working electrode was prepared by drop-casting 10 μg active material on a freshly polished GCE (polished with 0.05 μm alumina powder and rinsed by deionized water). Electrochemical impedance spectroscopy (EIS) was performed at the open-circuit voltage from 1 MHz to 1 Hz at a bias voltage of 5 mV. The calculation methods of the specific capacitance obtained from cyclic voltammetry (CV) and galvanostatic charge/discharge (GCD) curves are detailed in Supplementary data.

3. Results and discussion

3.1. Holey graphene fabrication

The schematic diagram of the two-step MACE method for holey graphene fabrication is illustrated in Fig. 1a. The bare GO aqueous solution is first pretreated under microwave irradiation for 90–360 s using a microwave reactor without any etchant, aiming to mildly reduce GO before etching. In the reduction of GO, when the oxygen-containing functional groups are removed from the graphene lattice, the surrounding carbon atoms can be taken away at the same time forming CO or CO_2 and leaving behind vacancies on the lattice [40]. Thus, the first-step processing can create single- and few-atom vacancy defects on GO sheets. Then, in the second step, the defected GO (dGO) solution is mixed with hydrogen peroxide and irradiated again in the microwave reactor for 45–180 s. Assisted by the microwave irradiation, the hydrogen peroxide molecules react with GO and remove carbon atoms from the lattice, especially the carbon atoms around vacancy defects since they are more chemically active [9,41,42]. The atom removal leads to the formation of nanoholes on the graphene basal plane. The ultra-high process efficiency is ascribed to the unique selective heating by microwave irradiation on the GO-etchant interface, which will be explained in the following sections. Eventually, a certain amount of hGO solution is obtained depending on the volume of the microwave reactor.

The morphology evolution of the pristine GO, dGO, and hGO sheets at different stages of fabrication were characterized by TEM. The pristine GO sheet (Fig. 1b) does not show any recognizable holey region on the basal plane, and the color of its aqueous solution is light brown (the inset in Fig. 1b). Within an area of the same size on the dGO sheet (Fig. 1c), two nanoholes with diameters of about 0.5 and 3.0 nm (the insets in Fig. 1c) are found, and the color of the dGO solution turns darker (the inset in Fig. 1c) due to the reduction of GO by the microwave pretreatment [43,44]. The yellow regions in the insets of Fig. 1c show that the functional groups are depleted in the areas around the nanoholes, while other areas on the dGO sheet are still covered by functional groups. This clearly suggests that the formation of the nanoholes on the dGO sheets are strongly related to the removal of functional groups. However, the sole reduction process (i.e., the removal of functional groups) cannot bring the formation of abundant nanoholes, and an etching reagent such as hydrogen peroxide is necessary. With the coupling effect of microwave irradiation and chemical etching, the nanoholes with a high density and diameters up to about 25 nm are observed on the basal plane of the hGO sheet (Fig. 1d). According to the AFM images (Fig. S2), no obvious change is identified from GO to hGO in both thickness (about 1 nm) and size (μm-scale), implying that both the microwave exposure and etchant concentration are in the appropriate ranges to avoid disintegrating the GO sheets into small pieces.

The XPS spectra of the pristine GO, dGO, and hGO sheets (Fig. 1e) show that they are mainly composed of C, O, S, and N atoms. By calculating the C/O or C/(O + N + S) atomic ratio from the XPS spectra, we can analyze the constituent change during each fabrication step. As indicated by the higher C/O ratio of dGO relative to GO (Fig. 1f), the microwave irradiation during the pretreatment causes a partial removal of the oxygen-containing functional groups from GO sheets. If the sulfur- and nitrogen-containing groups are considered, the pretreatment still brings an increase in terms of C/(O + N + S) from 2.05 to 2.23. After the MACE, the hGO sheets show a negligible increase of the C/O ratio from 2.40 to 2.41, suggesting that the losses of carbon and oxygen atoms were balanced during this step. The oxygen supply of hydrogen peroxide led to the formation of new oxygen-containing groups on GO sheets, equalizing the removal of oxygen-containing groups caused by the microwave irradiation. This is an obvious distinction between the MACE and conventional chemical-etching methods, which generally show a lower C/O ratio after etching [5,10,17,27]. The increase of the C/(O + N + S) ratio from 2.23 to 2.33 after the MACE indicates that the removal of sulfur- and nitrogen-containing groups on GO sheets are significant in this step.

Raman spectroscopy was employed to characterize the disorder level of GO sheets, i.e., the distortion of sp^2 graphitic rings on the graphene lattice affected by both defects and functional groups [45]. Research has reported that the disorder level of GO grows with the full width at half-maximum (FWHM) of the G band, one of the characteristic peaks in the Raman spectra of graphitic structures [46,47]. The FWHM(G) of GO (Fig. 1g) decreases from 66 to 63 cm^{-1} after the pretreatment and increases to 73 cm^{-1} after the MACE, suggesting that the graphitic arrangements of the graphene lattice are first restored by the pretreatment and then distorted by the MACE. Although the pretreatment creates the vacancy defects that distort the graphene lattice, the disorder level of dGO is affected more by the removal of functional groups during the pretreatment. The MACE, on the other hand, significantly promotes the disorder level by forming the nanoholes that cause large lattice distortion on hGO sheets. In addition, the intensity ratio of the D to G band (I_D/I_G) is another commonly used indicator of the disorder level on GO sheets. Cançado et al. report that with the increase of FWHM(G), the I_D/I_G ratio of the single-layer graphene first grows within a low-disorder range and then reduces when entering the high-disorder range [48]. In this study, the correlations between FWHM(G) and I_D/I_G (Fig. S3a) of all the GO, dGO, and hGO samples exhibit the similar trends. The values of FWHM(G) and I_D/I_G become lower from GO to dGO, while the hGO samples show mostly higher FWHM(G) and lower I_D/I_G than GO. It confirms that the dGO samples are in the low-disorder range where I_D/I_G increases with the disorder level, while the hGO samples are in the high-disorder range where I_D/I_G reduces with the disorder level. Also, it is found that FWHM(D) is a similar indicator as I_D/I_G to determine the disorder level of GO (Figs. S3b and S3c).

3.2. Controllable formation and growth of nanoholes

Differed from most solution-based methods of holey graphene fabrication [15–17,26–28], the two-step approach in this study can

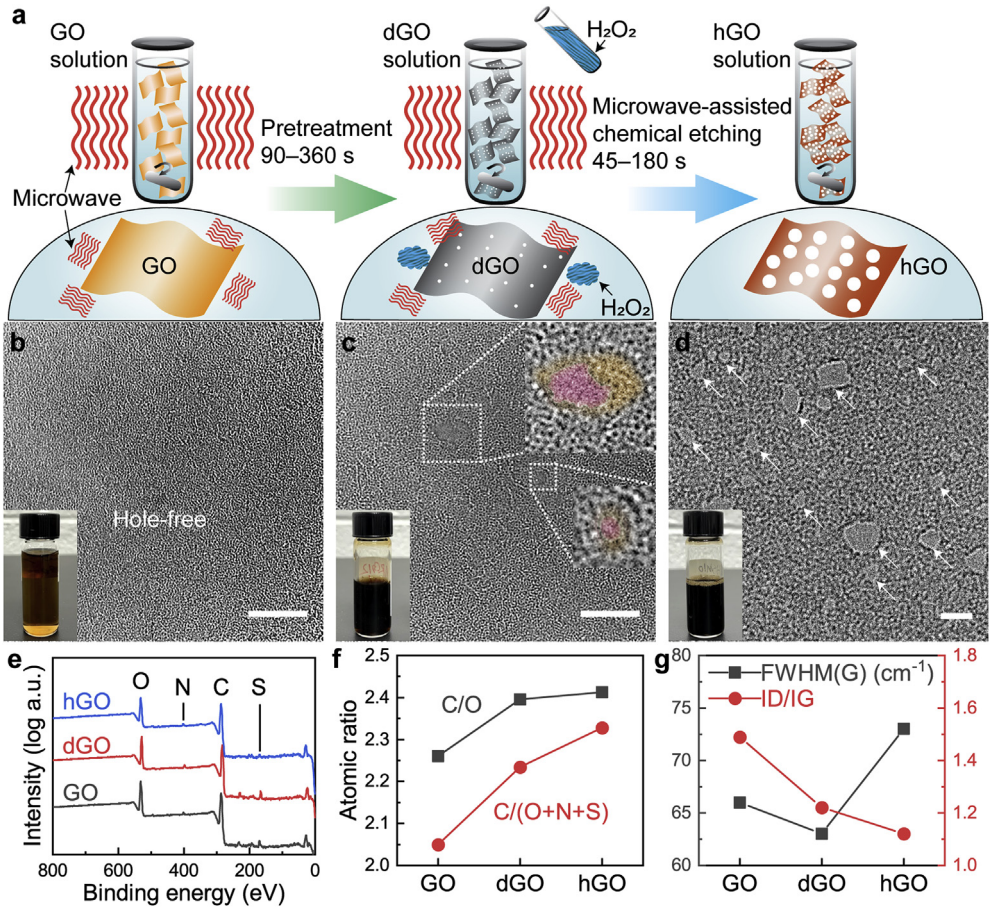

Fig. 1. Holey graphene fabrication via MACE with a two-step strategy. (a) Schematic of the fabrication process; TEM images of (b) pristine graphene oxide (GO), (c) defected graphene oxide (dGO), and (d) holey graphene oxide (hGO); (e) XPS spectra; (f) C/O and C/(O + N + S) atomic ratios obtained from XPS spectra; (g) full width at half-maximum of the G band (FWHM(G)) and intensity ratios of the D to G band (I_D/I_G) obtained from Raman spectra. Insets in the bottom-left corners of b–d are the digital images of the aqueous solutions. Insets in c magnify the locations of nanoholes and highlight the holes (red) and functional-group-depleted regions (yellow). Scale bars in b,c, 5 nm; in d, 20 nm. (A colour version of this figure can be viewed online.)

control the formation and growth of nanoholes by tuning the processing durations of the pretreatment and MACE. It enables microstructural engineering of holey graphene to meet requirements of various applications. To understand the effect of pretreatment on the size and population of nanoholes, a group of dGO samples were prepared with pretreatment duration of 90 (denoted as dGO-PS), 180 (denoted as dGO-PM), and 360 s (denoted as dGO-PL), respectively. After the MACE with the same condition (at 50 W for 90 s), the samples were denoted as hGO-PS, -PM, and -PL, respectively. Fig. 2a–c presents the TEM images of the hGO sheets. The statistics data of the nanoholes in these TEM images, including the total area percentage, population, range of diameter, median diameter, and average diameter, are collected (see values in Table S1) and compared in the radar chart (Fig. 2d).

With the shortest pretreatment, the TEM image of hGO-PS (Fig. 2a) displays a few sparsely scattered nanoholes with the range of diameter widely spread from 7 to 22 nm (Fig. S4a). The nanoholes of hGO-PS exhibit the lowest population (45 μm^{-2}) and area percentage (0.6%) because the 90-s pretreatment only creates a limited number of vacancy defects as the formation sites of nanoholes. The low defect density on the dGO-PS sheets is related to the low reduction level of dGO-PS indicated by the Raman (Fig. S3a) and XPS results (Fig. S5a) of dGO-PS: the C/O and C/(O + N + S) ratios of dGO-PS are the lowest among all the dGO-P samples; the decrease in I_D/I_G from GO (1.49) to dGO-PS (1.33) is also the smallest. As a result, the formation of nanoholes on the hGO-PS sheets is not prominent after the MACE. This can be also confirmed by the negligible increase in FWHM(G) from 64 to 66 cm^{-1} (Fig. 2e). Nevertheless, the nanoholes of hGO-PS have the largest average and median diameters (13.4 and 11 nm). During the MACE, the limited population of defect regions on the dGO-PS sheets causes the constant etching of a few preferential locations on the lattice where more carbon atoms are removed compared to the other samples.

With longer pretreatment, the nanohole population of hGO-PM drastically grows to 1687 μm^{-2}, bringing the high area percentage (2.1%) that generates the highest disorder level among all the samples (indicated by the largest FWHM(G) of 73 cm^{-1}, Fig. 2e). The nanoholes of hGO-PM exhibit the smallest values in the range of diameter (2.5–13.0 nm), average and median diameters (4.0 and 3.5 nm). As indicated by the lower FWHM(G) of dGO-PM relative to dGO-PS (Fig. 2e), the longer pretreatment causes a higher reduction level of dGO-PM, meaning the formation of more vacancy defects on the dGO-PM sheets. During the MACE, the dGO-PM sheets can provide many chemically active sites for the etching reaction, resulting in a uniform formation of abundant nanoholes on the hGO-PM sheets.

As the pretreatment duration increases to 360 s, the total area percentage of nanoholes of hGO-PL surges significantly to 6.0% with a large average diameter of 7.2 nm. As indicated by the largest C/O

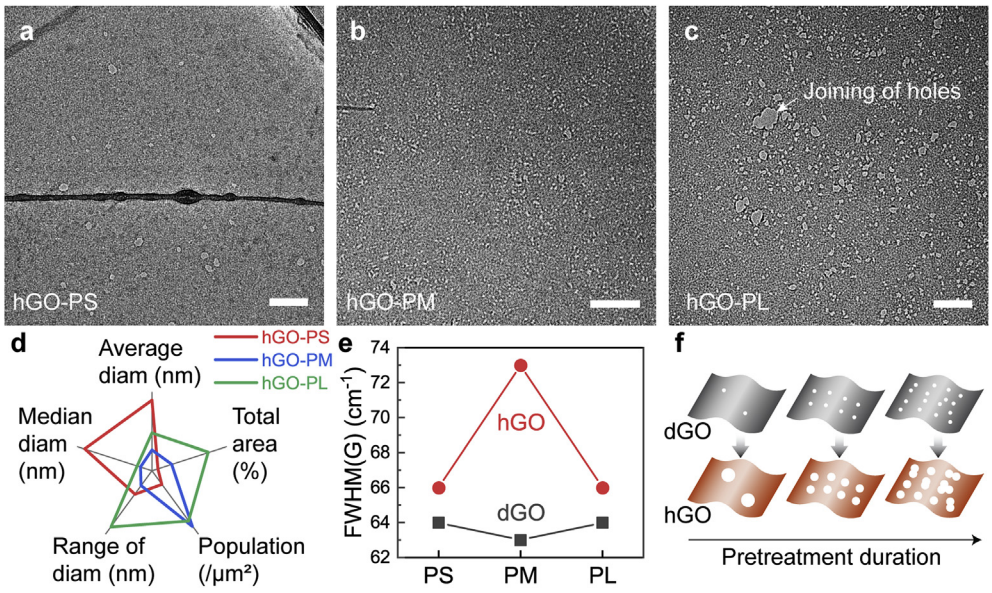

Fig. 2. Holey graphene oxide (hGO) sheets prepared with different pretreatment duration. TEM images of hGO pretreated for (a) 90, (b) 180, and (c) 360 s; (d) radar chart comparing the total area percentage, population, range of diameter, median diameter, and average diameter of the nanoholes in a–c; (e) FWHM(G) obtained from the Raman spectra vs. pretreatment durations of defected graphene oxide (dGO) and hGO; (f) schematic showing the effect of pretreatment on the microstructure of hGO. Scale bars in a–c, 100 nm. (A colour version of this figure can be viewed online.)

and C/(O + N + S) ratios (Fig. S5a) among all the dGO-P samples, the highest reduction level of dGO-PL leads to large numbers of defects created during the pretreatment, promoting the nanohole formation on the hGO-PL sheets. Many nanoholes joined each other during the MACE, forming much larger nanoholes with the diameters up to 53 nm (Fig. 2c). The joining of nanoholes leads to a slight drop in population and a broader range of diameter on hGO-PL relative to hGO-PM. However, the diameters of most nanoholes are still smaller than 5 nm (Fig. S4c). In fact, if we assume the average diameter of nanoholes is constant under a same processing condition during the MACE, a theoretical nanohole population (that has eliminated the effect of joining) of hGO-PL can be estimated using the average diameter of nanoholes of hGO-PM (4.0 nm) and the area percentage of hGO-PL (6.0%). The calculated value is 4775 μm^{-2}, much larger compared to hGO-PM (1687 μm^{-2}). It leads us to further consider the possibility of limiting the joining of nanoholes by varying the duration of MACE.

Fig. 2f illustrates the effect of pretreatment duration on the microstructure of nanoholes. With longer pretreatment, more functional groups can be removed from GO sheets, and a higher density of vacancy defects can be generated. During the MACE, these vacancy defects are constantly enlarged into nanoholes. Therefore, more nanoholes can be obtained on the hGO sheet with longer pretreatment. However, if the pretreatment is too long, the crowded nanoholes would join each other during the MACE, leading to the decrease of population. To effective tune the population of nanoholes, the MACE duration should be adjusted accordingly to control the growth of nanoholes.

To study the effect of MACE, another group of hGO sheets were prepared on the growth of nanoholes. The GO solutions were first pretreated under microwave for 180 s (the same as dGO-PM) to obtain a decent defect density on dGO as demonstrated above. Then, the dGO samples were etched for 45 s (denoted as hGO-ES), 90 s (denoted as hGO-EM), and 180 s (denoted as hGO-EM), respectively. TEM images of the hGO-E samples are shown in Fig. 3a–c, and the statistics data of the nanoholes are collected (Fig. S6) compared in the radar chart (Fig. 3d).

After the MACE of 45 s, small nanoholes (5.6 nm) are observed on hGO-ES with a relatively low population (454 μm^{-2}), while the range of diameter is narrow (3.5–18 nm). The emerging of nanoholes from vacancy defects is more obvious than the size growth of nanoholes. This is because that the short duration of MACE limits the etching of GO sheets. Both the C/O ratio (Fig. S5b) and FWHM(G) (Fig. 3e) show no obvious change caused by the short duration of MACE.

The longer MACE brings a drastic growth in the population of nanoholes to 1050 μm^{-2}. Compared to hGO-ES, hGO-EM shows a larger total area percentage of nanoholes (3.1%) and higher disorder level with FWHM(G) of 73 cm^{-1} (Fig. 3e). The range of nanohole diameter of hGO-PM become broader (3.5–31 nm) because of the joining and preferential growth of nanoholes during the 90-s MACE.

The MACE of 180 s results in a major boost both in the total area percentage (10.7%) and average diameter (10.3 nm) of nanoholes with a high population of 1295 μm^{-2}. The range of diameter further broadens (3.5–65 nm). Many joined holes with diameters over 20 nm are observed on the hGO-EL sheet (Fig. 3c). The disorder level of hGO-EL is the highest among all hGO-E samples, as indicated by FWHM(G) (Fig. 3e). Both the I_D/I_G (Fig. S3a) and C/O ratios (Fig. S5b) of hGO-EL abnormally increase after the MACE due to a higher reduction of GO induced by the microwave irradiation with long duration.

The mechanism of MACE is illustrated in Fig. 3f. In contrast to the effect of pretreatment, which mainly changes the population of nanoholes on hGO, the MACE process affects both the formation and growth of nanoholes by coupling chemical etching and microwave irradiation. With a moderate defect density on the dGO sheets, the longer duration of MACE brings a larger nanohole population but also the joining and preferential growth of nanoholes that increase the range of diameter and total area percentage. Therefore, the short duration of MACE is favorable to form the nanoholes with relatively uniform diameters, while the long duration of MACE contributes most to the high population and total area percentage of nanoholes. By tuning the duration of both pretreatment and MACE, the microstructural features of nanoholes can be effectively controlled.

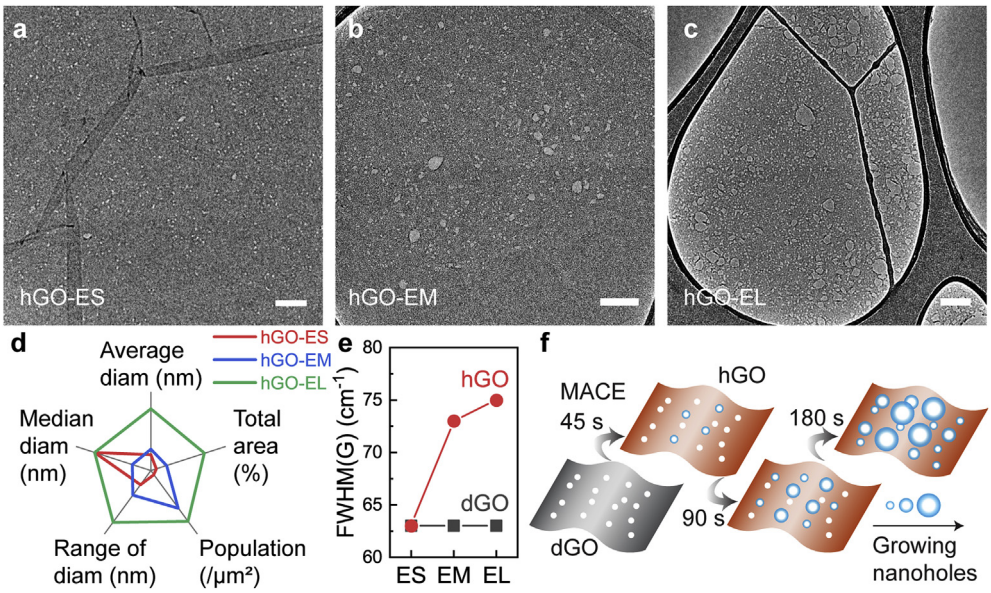

Fig. 3. Holey graphene oxide (hGO) prepared with different duration during microwave-assisted chemical etching (MACE). TEM images of hGO etched for (a) 45, (b) 90, and (c) 180 s; (d) radar chart comparing the total area percentage, population, range of diameter, median diameter, and average diameter of the nanoholes in a–c; (e) FWHM(G) obtained from the Raman spectra vs. pretreatment durations of defected graphene oxide (dGO) and hGO; (f) schematic of the effect of MACE on the microstructure of hGO. Scale bars in a–c, 100 nm. (A colour version of this figure can be viewed online.)

3.3. Thermal chemical mechanism of MACE

To unveil the thermal chemical mechanism during fabrication of holey graphene, the multiscale calculations based on the DFT and MD methods were carried out.

As demonstrated in the previous section, the in-plane vacancy defects formed during the microwave pretreatment of GO sheets is the key of tuning the size and population of nanoholes on hGO sheets, while how these defects affect the chemical etching process between graphene and hydrogen peroxide during the MACE remains unknown. To understand this process, we calculate the internal energy changes of the chemical interactions between one hydrogen peroxide molecule and graphene (Fig. 4a), GO (Fig. 4b), defected graphene (Fig. 4c), and dGO (Fig. 4d), respectively. We use a $6 \times 6 \times 1$ supercell to simulate the structure of graphene, adding to which epoxy models results in the GO structure. Each of the defected structure is obtained by removing a carbon atom from the center of the supercell. The calculation result shows that the hydrogen peroxide molecule cannot react with pure graphene or GO but can react with the defected graphene (−7.06 eV) or dGO (−7.03 eV). The reaction with the defected graphene produces a carbonyl, hydrogen, and hydroxyl group on the edge-sites of the vacancy defect. For dGO, a carbonyl group emerges at the same site, and two graphitic rings are broken due to a detached C—C bond. The results suggest that hydrogen peroxide can oxidize the defected graphene or GO sheets by adding oxygen-containing functional groups to the defected regions. The removal of carbon atoms that leads to the chemical etching of graphene or GO sheets is not

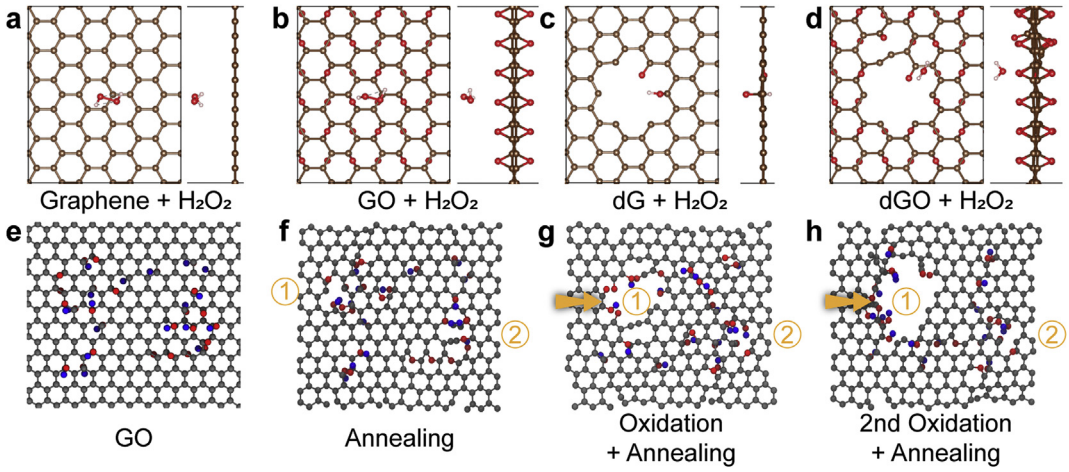

Fig. 4. Simulation results of the thermal chemical process during holey graphene fabrication based on density functional theory (DFT) and molecular dynamics (MD). DFT results of the reactions between one hydrogen peroxide molecule and (a) graphene, (b) GO, (c) defected graphene, and (d) defected GO, respectively. Results are presented in both front and side views. GO structures (e) at the start of the MD simulation, (f) after thermal annealing, (g) after further oxidation and annealing, and (h) after the second round of oxidation and annealing. The vacancy regions (or nanohole) are tagged with number 1 and 2. The arrows indicate the addition of functional groups in the designated region before thermal annealing. (A colour version of this figure can be viewed online.)

observed due to the zero-temperature limit in standard DFT calculation.

To further study the interaction between hydrogen peroxide and GO that couple both microwave-thermal and chemical effects, the classical MD simulation is conducted. The model of a single-layer GO sheet (Fig. 4e) is constructed using a periodical box of $3.4 \times 3.2 \times 6$ nm containing 11×11 unit cells. Epoxy and hydroxyl functional groups are randomly added on both sides of the GO sheet, and the oxygen concentration is 12.5%. The GO sheet is first annealed at 1000 K for 7.5 ps with a heat rate of 13 K fs^{-1} to mimic the microwave-thermal pretreatment. Note that, the annealing temperature herein is chosen according to a pre-fitted reactive force field (see methods section), which is not comparable to experimental temperature conditions. But, under the solely thermal effect, it is observed that several vacancy defects are created on GO (Fig. 4f) by the removal of carbon atoms and the breakage of C–C bonds. This confirms the pretreatment can lead to the formation of vacancy defects on GO by electromagnetic-wave-induced heating. The loss of carbon atoms or the breakage of C–C bonds on GO no longer occur after thermal annealing for a certain time (less than 2.5 ps). Therefore, the vacancy-to-nanohole transformation cannot be achieved by a solely thermal annealing. Per the results from the DFT calculations, additional hydroxyl and epoxy groups could be formed due to the oxidation effect of hydrogen peroxide and thus can be added to the edge-sites carbon atoms around the vacancy region (tagged with No. ① in Fig. 4f). For side by side comparison, another vacancy region (tagged with No. ② in Fig. 4f) is not added with any functional groups. Then, the model is annealed again under the same temperature for the same duration. The result (Fig. 4g) shows that the vacancy No. ① on GO is enlarged and transformed to a nanohole due to the loss of more carbon atoms and the breakage of more bonds until the functional groups are removed significantly. It suggests that the continuous growth of nanoholes on GO is caused by the coupling effect of both the electromagnetic-wave-induced heating and the oxidation by hydrogen peroxide. To confirm this idea, the addition of functional groups onto the edge-sites carbon atoms and the following annealing, are repeated for more cycles. As shown in Fig. 4h, the size of the nanohole No. ① grows further, while the No. ② vacancy remains the same size after the same treatment of thermal annealing but without any etchant oxidation or functional groups addition. These results of MD calculations clearly demonstrate that the formation of nanoholes originated from the cyclic etchant oxidation process occurring at the edge-sites atoms around pretreated vacancies on graphene basal plane. This agrees well with the experimental observation above, that the density and size of nanoholes can be effectively controlled by adjusting either the density of the pretreated vacancies or the oxidation cycles, in other words, the pretreatment duration or MACE duration.

3.4. Rapid fabrication enabled by selective heating

Besides the controllability of the nanohole features, our method provides a promising solution to scalable manufacturing of holey graphene by reducing the total processing time from hour-scale to minute-scale. The rapid process is attributed to the in situ heat generation of GO sheets under microwave irradiation. To understand the heating mechanism of this method, three samples with the same volume (3 mL), including deionized water and two dGO aqueous solutions with concentrations of 1 and 3 mg mL^{-1}, were irradiated under microwave with the same power and duration (50 W and 120 s) starting at room temperature. No etchant was added in any of the samples to avoid the effect of etching reaction. The final temperatures (Fig. 5a) are 140, 145, and 156 °C for the deionized water, 1 mg mL^{-1}, and 3 mg mL^{-1} dGO solutions, respectively, and the final pressures (Fig. 5b) of the three samples are 5.1, 5.7, and 7.7 bar, respectively. A higher dGO concentration leads to a greater energy absorption from the electromagnetic wave. In fact, the temperature rise of the dGO solutions should be composed of two parts: the temperature rise of water and that of dGO. In the 3 mg mL^{-1} dGO solution, the water of total 3 g brings a temperature rise of 115 °C, as indicated by the final temperature of deionized water, and thus the specific temperature rise per gram of water is 46.7 °C g^{-1}. Meanwhile, the dGO sheets of total 9 mg result in an extra temperature rise of 16 °C, and the specific temperature rise of dGO should be 1777.8 °C g^{-1}, over 30 times of that of water.

The plot of the temperature increase rates (the inset in Fig. 5a) suggests the heating can be divided into two stages: in stage I (0–50 s), the temperature increase rates of the three samples show no obvious difference and fluctuate at around 1.8 °C s^{-1}; in stage II (50–120 s), the temperature increase rates all drop to around 0.5 °C s^{-1}, while the solution with a higher dGO concentration can keep a faster increase. The lower heating rate in stage II mainly results from the heat loss for the evaporation of water starting at about 50 s. Another factor causing the lower heating rates in stage II could be the lower dielectric heating of water under higher temperatures [49]. Although the heating rates of the samples all reduce in stage II, the differences in heating rates among the samples become more obvious. This could be caused by the significant increase of the dielectric loss of GO above 100 °C [50]. With higher temperatures, the dielectric heating of water reduces, and that of dGO increases, leading to the greater differentiation in heating rates of the samples. Prior research has shown that the microwave can cause local electron movements in the π–π network on graphene sheets [51–53], resulting in the localized Joule heating that can generate high-temperature plasma arcs on graphene powders within 1–2 s [54]. This microwave-induced electronic heating is obviously different from the dielectric heating mechanism that generally relies on the dielectric loss of non-metallic polarized molecules. In this study, the dGO sheets can provide both the defects and functional groups for polar movements and the regional π–π networks for local electron movements [55]. Both dielectric heating and localized Joule heating could co-exist during microwave irradiation and cause intense heating on the surface of the dGO sheets. As a result, the dGO sheets in the solution can be selectively and efficiently heated by the microwave irradiation.

The actual temperature of the dGO sheets is difficult to be directly monitored during microwave irradiation. Nevertheless, under the consideration of the selective heating mechanism, the temperature of the dGO sheets in the solution during microwave irradiation can be calculated using an analytic model (see calculation details in Supplementary data). Briefly, the temperature rise of the solution or water is assumed to be determined by the microwave heating of water and dGO with no heat loss to the environment. Therefore, the heat solely generated by dGO sheets can be calculated. The higher temperature rise of dGO relative to water results in a heat conduction from the dGO sheets to their surrounding water molecules. Assuming the temperatures of dGO and water are equalized in each second, the temperature difference before equalization can be calculated using the heat generated by dGO per second. As shown in Fig. 5c, the results show that the temperature of the dGO sheets in the solutions is calculated to be constantly ~100 °C higher than the recorded temperatures of the solutions.

These results can be employed to demonstrate the mechanism involved in the rapid fabrication of holey graphene via MACE. The selective heating of GO sheets by microwave irradiation is the essential advantage of the MACE method over the conventional one. As shown in Fig. 5d, the conventional heating strongly depends on heat conduction and convection within the solution. The

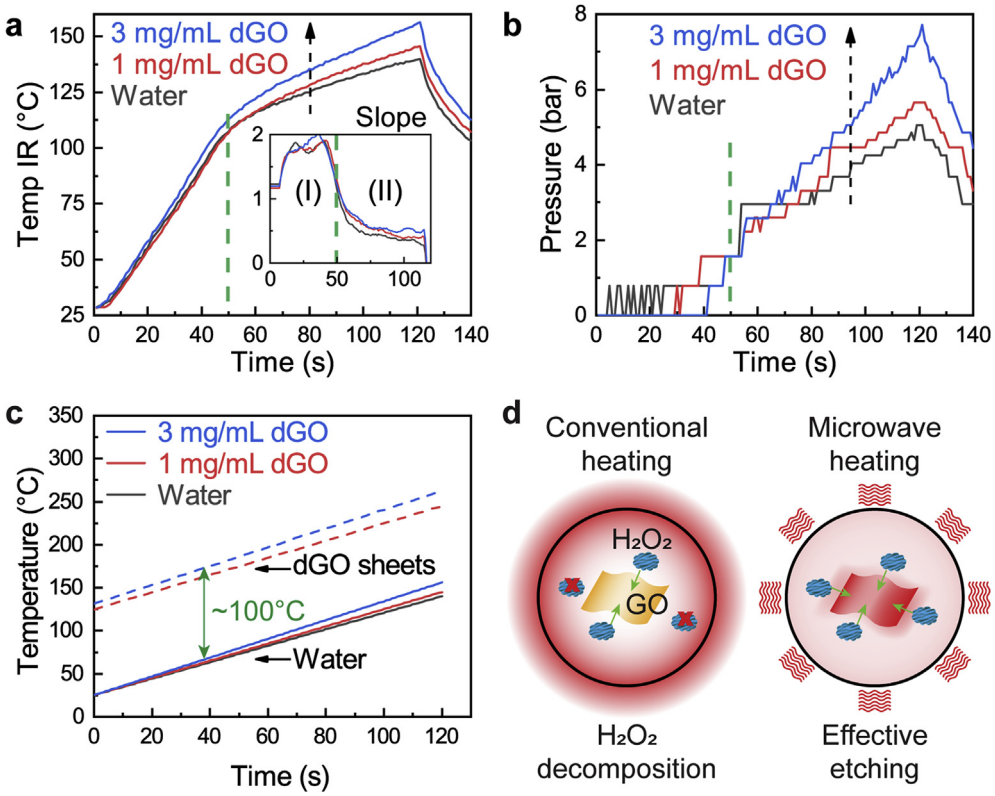

Fig. 5. Selective heating of defected graphene oxide (dGO) in aqueous solutions under microwave irradiation. (a) Temperature and (b) pressure profiles of deionized water and the dGO solutions of 1 and 3 mg mL^{-1} processed under the same microwave irradiation; (c) estimated temperatures of the dGO sheets in the solutions; (d) schematics of conventional heating and microwave heating of the GO aqueous solution with the addition of hydrogen peroxide. Inset in a shows the slope of temperature vs. time. (A colour version of this figure can be viewed online.)

heating of a GO sheet is achieved by heat conduction of its surrounding molecules. The hydrogen peroxide molecules can be decomposed before they can react with GO. In contrast, during the MACE, the GO sheets directly interact with microwave irradiation and quickly become the hot spots dispersed in the solution due to in situ heat generation, providing constant energy to facilitate the etching reaction with the surrounding hydrogen peroxide molecules. This implies both the process efficiency and controllability could be modulated by the microwave irradiation during the MACE process.

3.5. Capacitive performance

The capacitive performance of the holey graphene fabricated via MACE were measured in the 1 M Na_2SO_4 aqueous electrolyte with a three-electrode cell. Before electrochemical measurements, the hGO sheets were mildly reduced under microwave irradiation to enhance the electric conductivity by restoring π−π network on the lattice [43,56]. The mildly reduced hGO was denoted as rhGO. For comparison, the rGO electrode was also prepared by reducing GO sheets under the same condition. Fig. 6a show the CV curves of the rhGO and rGO electrodes obtained at a scan rate of 50 mV s^{-1} and a potential window from −0.2 to 0.8 V. As indicated by the enclosed areas of the CV curves, the specific capacitances of the rhGO electrodes are all higher than that of the rGO electrode (Table 1). The highest specific capacitance of rhGO is 111 F g^{-1}, about 3.5 times greater than that of rGO (32 F g^{-1}). Note that the capacitance of rGO here is relatively low compared to existing reports [57], owing to the mild reduction level of GO prepared without any additional agent. Nevertheless, this reduction level is enough to exhibit the significant improvement in capacitive performance brought by the nanoholes. In fact, both the double-layer capacitance and pseudo-capacitance contribute to the capacitive behavior of rhGO and rGO. Compared with rGO, rhGO can provide a larger accessible surface area for double-layer absorption and more electrochemically active sites to promote the pseudo-capacitance. Among the rhGO electrodes fabricated with different duration of pretreatment or MACE, rhGO-PM/EM with a high population and moderate area percentage of nanoholes shows the highest specific capacitance. Although both rhGO-PL and -EL have the population of nanoholes over 1000 μm^{-2}, their specific capacitances are lower than that of rhGO-PM/EM. The total area percentage of nanoholes on rhGO-PL or -EL is too high to provide a large surface area for double-layer capacitance.

Fig. 6b shows the GCD curves of the rhGO and rGO electrodes scanned at a current density of 10 A g^{-1} and a potential window from −0.2 to 0.8 V. All curves are close to the triangular shape, and their slopes in the low-voltage range become lower due to the enhancement of pseudo-capacitance. The specific capacitances (Table 1) calculated from the GCD curves agree well with the CV results. At a current density of 0.5 A g^{-1} (Fig. 6c), the specific capacitance of rhGO-PM/EM is 137 F g^{-1}, 4 times of that of rGO (33.8 F g^{-1}). When the current density increases to as high as 100 A g^{-1}, the rhGO-PM/EM electrode still retains a larger percentage (69%) of the highest specific capacitance relative to rGO (54%), suggesting a better rate capability of rhGO. This should result from the faster transport kinetics of electrolyte ions to the surface of the rhGO sheets.

The EIS measurements were employed to analyze the kinetic process of ion diffusion and charge transfer at the electrode-

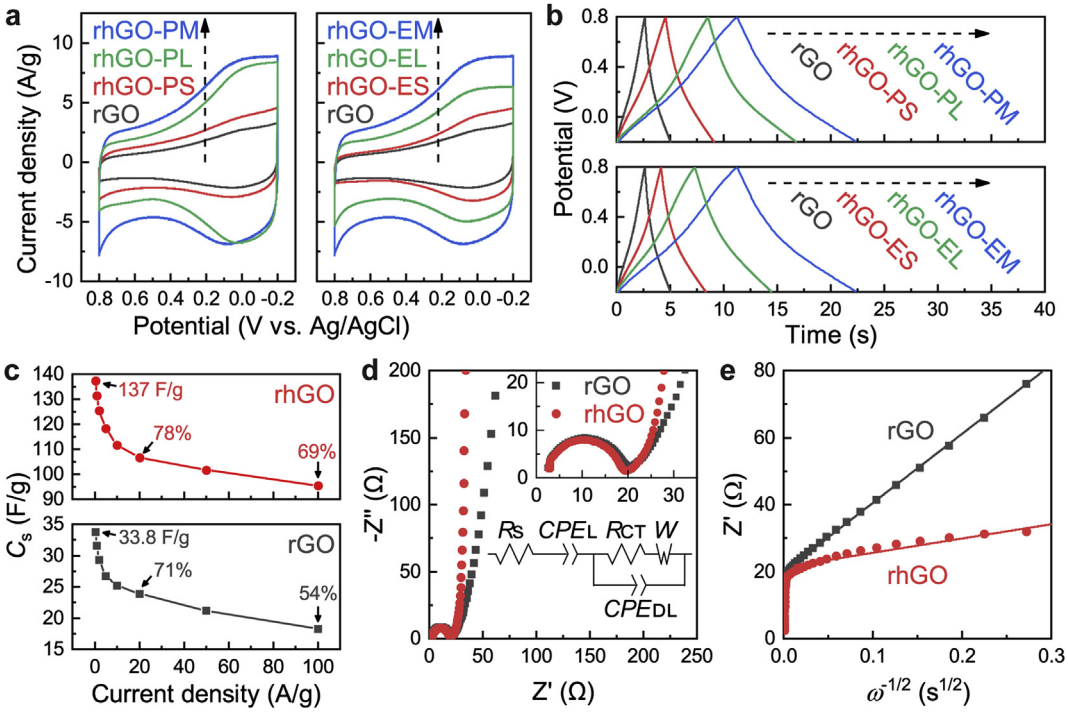

Fig. 6. Capacitive performance of reduced holey graphene oxide (rhGO) in 1 M Na_2SO_4. (a) CV curves at a scan rate of 50 mV s^{-1}; (b) GCD curves at a current density of 10 A g^{-1}; (c) specific capacitance calculated from the GCD curves vs. current density; (d) Nyquist plot; (e) Warburg plot. Insets in d are the equivalent circuit and the magnified plot in the high-frequency range. (A colour version of this figure can be viewed online.)

Table 1
Electrochemical properties of reduced holey graphene oxide (rhGO).

Sample	In sodium sulfate				In potassium ferricyanide			
	$C_{S,CV}$[a)] [F g^{-1}]	$C_{S,GCD}$[b)] [F g^{-1}]	R_{CT} [Ω]	D_W [× 10^{-9} cm^2 s^{-1}]	ΔE_P [mV]	R_{CT} [Ω]	$D_{R\text{-}S}$ [× 10^{-6} cm^2 s^{-1}]	D_W [× 10^{-6} cm^2 s^{-1}]
rGO	32	25	18	0.17	91	125	2.12 × 10^{-3}	4.20 × 10^{-4}
rhGO-PS	48	46	17	1.84	83	107	7.03	8.14
rhGO-PM	111	112	17	3.83	72	98	9.52	8.25
rhGO-PL	91	84	17	2.52	74	96	9.94	8.35
rhGO-ES	44	42	17	1.05	73	104	7.92	7.57
rhGO-EM	111	112	17	3.83	72	98	9.52	8.20
rhGO-EL	77	72	16	2.62	75	99	9.49	9.55

a) $C_{S,CV}$ is calculated from the CV curve measured at 50 mV s^{-1}.
b) $C_{S,GCD}$ is calculated from the GCD curve measured at 10 A g^{-1}.

electrolyte interface. In the Nyquist plot (Fig. 6d), the radius of the semicircle in the high-frequency range is proportional to the heterogeneous-charge-transfer resistance (R_{CT}) at the electrode/electrolyte interface, and the slope of the curve in the low-frequency range increase reversely with the Warburg resistance (W) reflecting the ion diffusion process [58,59]. The curves were fitted using the modified Randles circuit [60] (inset in Fig. 6d) that includes a resistor for the equivalent series resistance (R_S) composed of the solution resistance, contact resistance, and intrinsic resistance of the electrode, a constant phase element due to the limit capacitance (CPE_L), a CPE due to the double-layer capacitance (CPE_{DL}), a resistor for R_{CT}, and a Warburg impedance element (W). The R_S values in the rhGO and rGO electrodes are within a small range of 2.3–2.4 Ω, because the solution and contact resistances and the reduction level of all samples are the same. The rhGO and rGO electrodes also have similar R_{CT} values of 16–18 Ω (Table 1), while the rhGO electrodes display higher slopes in the low-frequency range (Figs. 6d and S9), indicating a faster diffusion-controlled process. To quantify the ion diffusion kinetics in the rhGO and rGO electrodes, the ion diffusion coefficient can be obtained via [15,17,58].

$$D_W = \left[RT \Big/ \left(n^2F^2Ac\sigma_W\right)\right]^2 \Big/ 2 \quad (1)$$

where D_W is the ion diffusion coefficient (cm^2 s^{-1}) calculated using the Warburg coefficient σ_W (Ω $s^{-1/2}$), R is the gas constant (J K^{-1} mol^{-1}), T is temperature (K), n is the number of electron transfer (here is 1), F is the Faraday constant (C mol^{-1}), A is the geometric surface area of the electrode (cm^2), and c is the concentration of Na^+ ions (mol ml^{-1}). σ_W can be further obtained from Ref. [58].

$$Z' = (R_S + R_{CT}) + \sigma_W\omega^{-1/2} \quad (2)$$

where Z' is the real part of the impedance (Ω) and ω is the frequency (s^{-1}). By plotting Z' versus $\omega^{-1/2}$ (i.e., the Warburg plot), σ_W can be calculated from the slope of the curve in the low-frequency range. Per Equations (1) and (2), a lower slope in the Warburg plot results in a smaller σ_W and higher D_W. As shown in Figs. 6e and S10, all the

rhGO electrodes have lower slopes relative to the rGO counterpart. The calculation results (Table 1) show that all the D_W values of rhGO are an order of magnitude higher than that of rGO. Among them, rhGO-PM/EM exhibits the highest value of 3.83×10^{-9} cm^2 s^{-1}, about 20 times larger than that of rGO (0.17×10^{-9} cm^2 s^{-1}). It clearly demonstrates that the nanoholes significantly facilitates the ion diffusion kinetics by providing abundant ion transport shortcuts through the rhGO sheets. Among the rhGO electrodes with different duration of pretreatment and MACE, the trend of D_W agrees well with that of specific capacitance calculated from both the CV and GCD curves. The large population and moderate area percentage of nanoholes on rhGO are favorable to improve the accessible surface area and ion diffusion kinetics.

3.6. Electrochemical catalytic activity

CV and EIS of the rhGO electrodes measured in the 5 mM $K_3[Fe(CN)_6]$ and 0.1 M KCl aqueous electrolyte can be used to evaluate the electrochemical catalytic activity of rhGO in redox reactions. As shown in Fig. 7a and b, the redox peaks near 0.2 V are observed in all the CV curves of rhGO and rGO. During a negative scan, $[Fe(CN)_6]^{3-}$ ions are reduced to $[Fe(CN)_6]^{4-}$ ions by capturing electrons from the electrode, causing a cathodic current peak; during a positive scan, $[Fe(CN)_6]^{4-}$ ions are oxidized to $[Fe(CN)_6]^{3-}$ ions, generating an anodic current peak [61]. The rhGO electrodes exhibit remarkably higher catalytic activity compared to the rGO counterpart, as indicated by the 40 times higher redox peaks in the CV curves at a scan rate of 10 mV s^{-1}. Among the rhGO electrodes (insets in Fig. 7a and b), the redox peak grows with the area percentage of nanoholes. Higher redox peaks result from both faster redox kinetics and diffusion kinetics. Firstly, more electrochemically active sites around the nanoholes contribute to faster redox kinetics by providing a larger electronic density of states of the electrode material [62]. It can be confirmed by the variation of peak-to-peak separation (ΔE_P) in the CV curves of different rhGO electrodes (Table 1). The rhGO electrodes with a higher area percentage of nanoholes tend to have smaller ΔE_P, meaning that a lower driving potential is required to trigger the redox reactions. Thus, the high area percentage of nanoholes are beneficial to the faster heterogeneous electron transfer. Secondly, the nanoholes on rhGO provide abundant shortcuts for ion transportation, leading to faster diffusion kinetics. When ions participate in redox reactions, a diffusion layer gradually forms, where redox reactants are depleted, and further redox reactions are controlled by the ion diffusion rate [61]. In rhGO, ions transport via nanoholes and thus can deliver charges on the rhGO sheets located deeper from the electrode surface, causing a part of the diffusion layer overlapped by the depth of the rhGO electrode. Therefore, compared to the rGO counterpart, the diffusion layer above the surface of the rhGO electrode should be thinner, which facilitates the ion diffusion. The ion diffusion coefficient can be given by the Randles-Sevcik equation [9,58,59,61].

$$i_p = 0.4463\, n^{\frac{3}{2}} F^{\frac{3}{2}} A c (\nu D_{R-S}/RT)^{1/2} \quad (3)$$

where i_p is the peak current (A), n is the number of electron transfer (here is 1), c is the concentration of $[Fe(CN)_6]^{3-}$ ions (mol ml^{-1}), ν is the scan rate (V s^{-1}), and $D_{R\text{-}S}$ represents the diffusion coefficient (cm^2 s^{-1}) of $[Fe(CN)_6]^{3-}$ ions calculated from the Randles-Sevcik equation. By plotting i_P versus $\nu^{1/2}$ (i.e., the Randles-Sevcik plot), the ion diffusion coefficient can be calculated from Equation (3) using the slope of the curve. As shown in Figs. 7c and S12, good linear correlations between i_P and $\nu^{1/2}$ are observed in all samples. The calculation results (Table 1) based on Equation (3) show that the ion diffusion coefficients in rhGO are at least three orders of magnitude higher than that in rGO (2.12×10^{-9} cm^2 s^{-1}). The rhGO-PL electrode has the highest ion diffusion coefficients of 9.94×10^{-6} cm^2 s^{-1}. The ion diffusion rate increases with the area

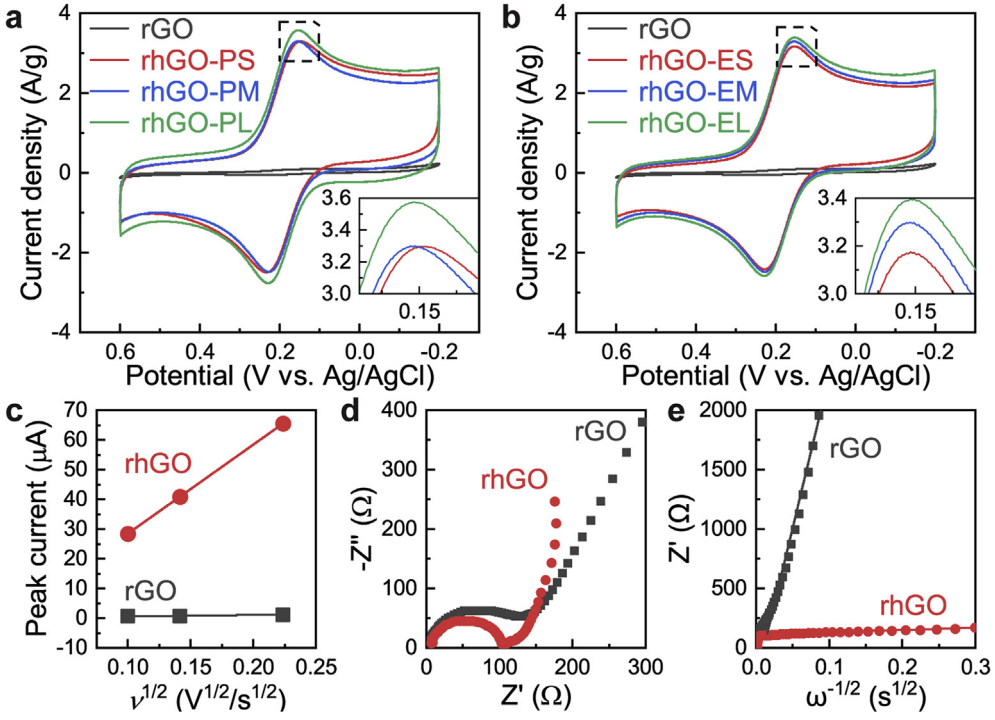

Fig. 7. Electrochemical catalytic activity of reduced holey graphene oxide (rhGO) in 5 mM $K_3[Fe(CN)_6]$ and 0.1 M KCl: (a,b) CV curves at a scan rate of 10 mV s^{-1}; (c) Randles-Sevcik plot measured at scan rates of 10–50 mV s^{-1}; (d) Nyquist plot; (e) Warburg plot. Insets in a,b respectively magnify the positive redox peaks indicated by the dash lines. (A colour version of this figure can be viewed online.)

percentage of nanoholes on rhGO, except for rhGO-EL that shows a slight drop compared with rhGO-EM.

The EIS Nyquist plot shown in Fig. 7d further demonstrates the distinct redox kinetics and diffusion kinetics between rhGO and rGO, as indicated by different behaviors in both high- and low-frequency ranges. As shown in Table 1, the values of R_{CT} in rhGO are all at least 20 Ω smaller than that in rGO, confirming the faster heterogeneous electron transfer on rhGO relative to rGO. Among the rhGO electrodes, the heterogeneous electron transfer becomes faster with increasing area percentage of nanoholes, and the only exception is rhGO-EL that shows a slight drop. This is consistent with the trend of $D_{R\text{-}S}$. In addition, the diffusion kinetics can be quantified with the EIS data using the Warburg plot. As shown in Fig. 7e, rhGO-PL shows a much lower slope in the Warburg plot compared to rGO, suggesting a smaller Warburg coefficient. The calculation results (Table 1) of ion diffusion coefficients based on Equations (1) and (2) agree well with those obtained based on Equation (3). These results confirm again that the high area percentage of nanoholes can improve the catalytic activity by providing more electrochemically active sites.

4. Conclusion

The fabrication of holey graphene with excellent capacitive performance and electrochemical catalytic activity was achieved within a few minutes via the MACE method, which was much faster than conventional hour-scale approaches. Moreover, the population, average diameter, area percentage of nanoholes on holey graphene sheets were effectively controlled by a two-step strategy combining pretreatment and MACE to further promote the electrochemical properties. This microwave-assisted method was fast, controllable, totally solution-based, and thus favorable to be employed in large-scale manufacturing for various applications.

The structural characterizations provided insights into the nucleation and growth of nanoholes during each step of fabrication. The pretreatment caused a partial reduction of GO sheets with an increased defect density. DFT and MD simulations confirmed that the vacancy defects can grow into nanoholes in MACE process due to the coupling effect of microwave irradiation and hydrogen peroxide oxidation. We also elucidated the mechanism of the rapid fabrication process. During the MACE, the microwave-induced selective heating of GO sheets by both localized Joule heating and dielectric heating, which facilitated the effective etching of GO sheets and limited the decomposition of hydrogen peroxide during processing. In electrochemical measurements, the nanoholes on holey graphene significantly improved the accessible surface area of the electrode, heterogeneous electron transfer, and ion diffusion kinetics, demonstrating the great application potential of the microwave-fabricated holey graphene in the fields of energy storage and electrochemical catalysis.

Declaration of competing interest

The authors declare that they have no known competing financial interests or personal relationships that could have appeared to influence the work reported in this paper.

CRediT authorship contribution statement

Dini Wang: Conceptualization. **Rui Dai:** Conceptualization. **Xing Zhang:** Conceptualization. **Lei Liu:** Conceptualization. **Houlong Zhuang:** Writing - review & editing. **Yongfeng Lu:** Writing - review & editing. **Yan Wang:** Writing - review & editing. **Yiliang Liao:** Writing - review & editing. **Qiong Nian:** Writing - review & editing.

Acknowledgements

This study is partially supported by Arizona State University startup funds, NSF grant CMMI-1825576. We acknowledge the use of facilities within the Eyring Materials Center at Arizona State University supported in part by NNCI-ECCS-1542160. This research also used computational resources of the Texas Advanced Computing Center under contract no. TG-DMR170070. We also appreciate the assistance of Dr. Q. H. Wang and her group members in Raman spectroscopy study.

Appendix A. Supplementary data

Supplementary data to this article can be found online at https://doi.org/10.1016/j.carbon.2020.01.076.

References

[1] K.S. Novoselov, V.I. Fal'ko, L. Colombo, P.R. Gellert, M.G. Schwab, K. Kim, A roadmap for graphene, Nature 490 (7419) (2012) 192–200.
[2] T. Wang, D. Huang, Z. Yang, S. Xu, G. He, X. Li, N. Hu, G. Yin, D. He, L. Zhang, A review on graphene-based gas/vapor sensors with unique properties and potential applications, Nano-Micro Lett. 8 (2) (2016) 95–119.
[3] H. Wang, T. Maiyalagan, X. Wang, Review on recent progress in nitrogen-doped graphene: synthesis, characterization, and its potential applications, ACS Catal. 2 (5) (2012) 781–794.
[4] X. Han, Z. Yang, B. Zhao, S. Zhu, L. Zhou, J. Dai, J.-W. Kim, B. Liu, J.W. Connell, T. Li, B. Yang, Y. Lin, L. Hu, Compressible, dense, three-dimensional holey graphene monolithic architecture, ACS Nano 11 (3) (2017) 3189–3197.
[5] Y. Xu, Z. Lin, X. Zhong, X. Huang, N.O. Weiss, Y. Huang, X. Duan, Holey graphene frameworks for highly efficient capacitive energy storage, Nat. Commun. 5 (2014) 4554.
[6] R. Raccichini, A. Varzi, S. Passerini, B. Scrosati, The role of graphene for electrochemical energy storage, Nat. Mater. 14 (3) (2015) 271.
[7] Y. Sun, Q. Wu, G. Shi, Graphene based new energy materials, Energy Environ. Sci. 4 (4) (2011) 1113–1132.
[8] M. Pumera, Graphene-based nanomaterials and their electrochemistry, Chem. Soc. Rev. 39 (11) (2010) 4146–4157.
[9] W. Yuan, Y. Zhou, Y. Li, C. Li, H. Peng, J. Zhang, Z. Liu, L. Dai, G. Shi, The edge- and basal-plane-specific electrochemistry of a single-layer graphene sheet, Sci. Rep. 3 (2013) 2248.
[10] H. Sun, L. Mei, J. Liang, Z. Zhao, C. Lee, H. Fei, M. Ding, J. Lau, M. Li, C. Wang, X. Xu, G. Hao, B. Papandrea, I. Shakir, B. Dunn, Y. Huang, X. Duan, Three-dimensional holey-graphene/niobia composite architectures for ultrahigh-rate energy storage, Science 356 (6338) (2017) 599–604.
[11] E. Alsharaeh, F. Ahmed, Y. Aldawsari, M. Khasawneh, H. Abuhimd, M. Alshahrani, Novel synthesis of holey reduced graphene oxide (HRGO) by microwave irradiation method for anode in lithium-ion batteries, Sci. Rep. 6 (2016) 29854.
[12] X. Zhao, C.M. Hayner, M.C. Kung, H.H. Kung, Flexible holey graphene paper electrodes with enhanced rate capability for energy storage applications, ACS Nano 5 (11) (2011) 8739–8749.
[13] E.D. Walsh, X. Han, S.D. Lacey, J.-W. Kim, J.W. Connell, L. Hu, Y. Lin, Dry-processed, binder-free holey graphene electrodes for supercapacitors with ultrahigh areal loadings, ACS Appl. Mater. Interfaces 8 (43) (2016) 29478–29485.
[14] X. Han, M.R. Funk, F. Shen, Y.-C. Chen, Y. Li, C.J. Campbell, J. Dai, X. Yang, J.-W. Kim, Y. Liao, J.W. Connell, V. Barone, Z. Chen, Y. Lin, L. Hu, Scalable holey graphene synthesis and dense electrode fabrication toward high-performance ultracapacitors, ACS Nano 8 (8) (2014) 8255–8265.
[15] S. Zhai, C. Wang, H.E. Karahan, Y. Wang, X. Chen, X. Sui, Q. Huang, X. Liao, X. Wang, Y. Chen, Nano-RuO2-Decorated holey graphene composite fibers for micro-supercapacitors with ultrahigh energy density, Small 14 (29) (2018) 1800582.
[16] J. Zhao, Y.-Z. Zhang, F. Zhang, H. Liang, F. Ming, H.N. Alshareef, Z. Gao, Partially reduced holey graphene oxide as high performance anode for sodium-ion batteries, Adv. Energy Mater. 9 (7) (2019) 1803215.
[17] C. Zhu, Z. Hui, H. Pan, S. Zhu, Q. Zhang, J. Mao, Z. Guo, Y. Li, M. Imtiaz, Z. Chen, Ultrafast Li-ion migration in holey-graphene-based composites constructed by a generalized ex situ method towards high capacity energy storage, J. Mater. Chem. 7 (9) (2019) 4788–4796.
[18] Q. Zheng, Y. Geng, S. Wang, Z. Li, J.-K. Kim, Effects of functional groups on the mechanical and wrinkling properties of graphene sheets, Carbon 48 (15) (2010) 4315–4322.
[19] T.H. Han, Y.-K. Huang, A.T. Tan, V.P. Dravid, J. Huang, Steam etched porous graphene oxide network for chemical sensing, J. Am. Chem. Soc. 133 (39) (2011) 15264–15267.
[20] X. Wang, L. Jiao, K. Sheng, C. Li, L. Dai, G. Shi, Solution-processable graphene nanomeshes with controlled pore structures, Sci. Rep. 3 (2013) 1996.

[21] Y. Zhu, S. Murali, M.D. Stoller, K. Ganesh, W. Cai, P.J. Ferreira, A. Pirkle, R.M. Wallace, K.A. Cychosz, M. Thommes, Carbon-based supercapacitors produced by activation of graphene, Science 332 (6037) (2011) 1537–1541.
[22] Y. Lin, K.A. Watson, J.-W. Kim, D.W. Baggett, D.C. Working, J.W. Connell, Bulk preparation of holey graphene via controlled catalytic oxidation, Nanoscale 5 (17) (2013) 7814–7824.
[23] Y. Zhao, C. Hu, L. Song, L. Wang, G. Shi, L. Dai, L. Qu, Functional graphene nanomesh foam, Energy Environ. Sci. 7 (6) (2014) 1913–1918.
[24] J.G. Radich, P.V. Kamat, Making graphene holey. Gold-nanoparticle-mediated hydroxyl radical attack on reduced graphene oxide, ACS Nano 7 (6) (2013) 5546–5557.
[25] Y. Xu, C.-Y. Chen, Z. Zhao, Z. Lin, C. Lee, X. Xu, C. Wang, Y. Huang, M.I. Shakir, X. Duan, Solution processable holey graphene oxide and its derived macrostructures for high-performance supercapacitors, Nano Lett. 15 (7) (2015) 4605–4610.
[26] M. Kotal, H. Kim, S. Roy, I. Oh, Sulfur and nitrogen Co-doped holey graphene aerogel for structurally resilient solid-state supercapacitors under high-compressions, J. Mater. Chem. 5 (33) (2017) 17253–17266.
[27] J. Liu, P. Du, Q. Wang, D. Liu, P. Liu, Mild synthesis of holey N-doped reduced graphene oxide and its double-edged effects in polyaniline hybrids for supercapacitor application, Electrochim. Acta 305 (2019) 175–186.
[28] C. Wang, S. Zhai, Z. Yuan, J. Chen, X. Zhang, Q. Huang, Y. Wang, X. Liao, L. Wei, Y. Chen, A core-sheath holey graphene/graphite composite fiber intercalated with MoS2 nanosheets for high-performance fiber supercapacitors, Electrochim. Acta 305 (2019) 493–501.
[29] S.D. Lacey, E.D. Walsh, E. Hitz, J. Dai, J.W. Connell, L. Hu, Y. Lin, Highly compressible, binderless and ultrathick holey graphene-based electrode architectures, Nanomater. Energy 31 (2017) 386–392.
[30] D.J. Kirsch, S.D. Lacey, Y. Kuang, G. Pastel, H. Xie, J.W. Connell, Y. Lin, L. Hu, Scalable dry processing of binder-free lithium-ion battery electrodes enabled by holey graphene, ACS Appl. Energy Mater. 2 (5) (2019) 2990–2997.
[31] Y.-Y. Peng, Y.-M. Liu, J.-K. Chang, C.-H. Wu, M.-D. Ger, N.-W. Pu, C.-L. Chang, A facile approach to produce holey graphene and its application in supercapacitors, Carbon 81 (2015) 347–356.
[32] M. Patel, W. Feng, K. Savaram, M.R. Khoshi, R. Huang, J. Sun, E. Rabie, C. Flach, R. Mendelsohn, E. Garfunkel, H. He, Microwave enabled one-pot, one-step fabrication and nitrogen doping of holey graphene oxide for catalytic applications, Small 11 (27) (2015) 3358–3368.
[33] K. Savaram, M. Li, K. Tajima, K. Takai, T. Hayashi, G. Hall, E. Garfunkel, V. Osipov, H. He, Dry microwave heating enables scalable fabrication of pristine holey graphene nanoplatelets and their catalysis in reductive hydrogen atom transfer reactions, Carbon 139 (2018) 861–871.
[34] L. Lin, H. Peng, Z. Liu, Synthesis challenges for graphene industry, Nat. Mater. 18 (6) (2019) 520–524.
[35] D.C. Marcano, D.V. Kosynkin, J.M. Berlin, A. Sinitskii, Z. Sun, A. Slesarev, L.B. Alemany, W. Lu, J.M. Tour, Improved synthesis of graphene oxide, ACS Nano 4 (8) (2010) 4806–4814.
[36] G. Kresse, J. Furthmüller, Efficiency of ab-initio total energy calculations for metals and semiconductors using a plane-wave basis set, Comput. Mater. Sci. 6 (1) (1996) 15–50.
[37] J.P. Perdew, K. Burke, M. Ernzerhof, Generalized gradient approximation made simple, Phys. Rev. Lett. 77 (18) (1996) 3865–3868.
[38] G. Kresse, D. Joubert, From ultrasoft pseudopotentials to the projector augmented-wave method, Phys. Rev. B 59 (3) (1999) 1758–1775.
[39] P.E. Blöchl, Projector augmented-wave method, Phys. Rev. B 50 (24) (1994) 17953–17979.
[40] A. Bagri, C. Mattevi, M. Acik, Y.J. Chabal, M. Chhowalla, V.B. Shenoy, Structural evolution during the reduction of chemically derived graphene oxide, Nat. Chem. 2 (2010) 581.
[41] A. Kumatani, C. Miura, H. Kuramochi, T. Ohto, M. Wakisaka, Y. Nagata, H. Ida, Y. Takahashi, K. Hu, S. Jeong, J.-i. Fujita, T. Matsue, Y. Ito, Chemical dopants on edge of holey graphene accelerate electrochemical hydrogen evolution reaction, Adv. Sci. 6 (10) (2019) 1900119.
[42] S. Banerjee, J. Shim, J. Rivera, X. Jin, D. Estrada, V. Solovyeva, X. You, J. Pak, E. Pop, N. Aluru, R. Bashir, Electrochemistry at the edge of a single graphene layer in a nanopore, ACS Nano 7 (1) (2013) 834–843.
[43] Y. Zhu, S. Murali, M.D. Stoller, A. Velamakanni, R.D. Piner, R.S. Ruoff, Microwave assisted exfoliation and reduction of graphite oxide for ultracapacitors, Carbon 48 (7) (2010) 2118–2122.
[44] W.F. Chen, L.F. Yan, P.R. Bangal, Preparation of graphene by the rapid and mild thermal reduction of graphene oxide induced by microwaves, Carbon 48 (4) (2010) 1146–1152.
[45] K.N. Kudin, B. Ozbas, H.C. Schniepp, R.K. Prud'homme, I.A. Aksay, R. Car, Raman spectra of graphite oxide and functionalized graphene sheets, Nano Lett. 8 (1) (2008) 36–41.
[46] A.C. Ferrari, D.M. Basko, Raman spectroscopy as a versatile tool for studying the properties of graphene, Nat. Nanotechnol. 8 (4) (2013) 235–246.
[47] M.S. Dresselhaus, A. Jorio, M. Hofmann, G. Dresselhaus, R. Saito, Perspectives on carbon nanotubes and graphene Raman spectroscopy, Nano Lett. 10 (3) (2010) 751–758.
[48] L.G. Cançado, A. Jorio, E.H.M. Ferreira, F. Stavale, C.A. Achete, R.B. Capaz, M.V.O. Moutinho, A. Lombardo, T.S. Kulmala, A.C. Ferrari, Quantifying defects in graphene via Raman spectroscopy at different excitation energies, Nano Lett. 11 (8) (2011) 3190–3196.
[49] M. Tanaka, M. Sato, Microwave heating of water, ice, and saline solution: molecular dynamics study, J. Chem. Phys. 126 (3) (2007), 034509.
[50] X. Huang, C. Zhi, P. Jiang, D. Golberg, Y. Bando, T. Tanaka, Temperature-dependent electrical property transition of graphene oxide paper, Nanotechnology 23 (45) (2012) 455705.
[51] W.-S. Jiang, C. Yang, G.-X. Chen, X.-Q. Yan, S.-N. Chen, B.-W. Su, Z.-B. Liu, J.-G. Tian, Preparation of high-quality graphene using triggered microwave reduction under an air atmosphere, J. Mater. Chem. C 6 (7) (2018) 1829–1835.
[52] H. Hu, Z. Zhao, Q. Zhou, Y. Gogotsi, J. Qiu, The role of microwave absorption on formation of graphene from graphite oxide, Carbon 50 (9) (2012) 3267–3273.
[53] S. Kang, H. Choi, S.B. Lee, S.C. Park, J.B. Park, S. Lee, Y. Kim, B.H. Hong, Efficient heat generation in large-area graphene films by electromagnetic wave absorption, 2D Mater. 4 (2) (2017), 025037.
[54] D. Voiry, J. Yang, J. Kupferberg, R. Fullon, C. Lee, H.Y. Jeong, H.S. Shin, M. Chhowalla, High-quality graphene via microwave reduction of solution-exfoliated graphene oxide, Science 353 (6306) (2016) 1413–1416.
[55] C. Wang, X. Han, P. Xu, X. Zhang, Y. Du, S. Hu, J. Wang, X. Wang, The electromagnetic property of chemically reduced graphene oxide and its application as microwave absorbing material, Appl. Phys. Lett. 98 (7) (2011), 072906.
[56] Y. Zhu, M.D. Stoller, W. Cai, A. Velamakanni, R.D. Piner, D. Chen, R.S. Ruoff, Exfoliation of graphite oxide in propylene carbonate and thermal reduction of the resulting graphene oxide platelets, ACS Nano 4 (2) (2010) 1227–1233.
[57] F. Bonaccorso, L. Colombo, G. Yu, M. Stoller, V. Tozzini, A.C. Ferrari, R.S. Ruoff, V. Pellegrini, Graphene, related two-dimensional crystals, and hybrid systems for energy conversion and storage, Science 347 (6217) (2015) 1246501.
[58] A.J. Bard, L.R. Faulner, Electrochemical Methods: Fundamentals and Applications, 2rd ed., Wiley, New York, 2001.
[59] P. Zanello, Inorganic Electrochemistry: Theory, Practice and Application, The Royal Society of Chemistry, Cambridge, UK, 2003.
[60] J.E.B. Randles, Kinetics of rapid electrode reactions, Discuss. Faraday Soc. 1 (1947) 11–19, 0.
[61] N. Elgrishi, K.J. Rountree, B.D. McCarthy, E.S. Rountree, T.T. Eisenhart, J.L. Dempsey, A practical beginner's guide to cyclic voltammetry, J. Chem. Educ. 95 (2) (2018) 197–206.
[62] N.G. Shang, P. Papakonstantinou, M. McMullan, M. Chu, A. Stamboulis, A. Potenza, S.S. Dhesi, H. Marchetto, Catalyst-free efficient growth, orientation and biosensing properties of multilayer graphene nanoflake films with sharp edge planes, Adv. Funct. Mater. 18 (21) (2008) 3506–3514.